Title

Angle-resolved Photoemission Extended Fine Structure of the Ni 3p, Cu3s, and Cu 3p core levels of the respective clean (111) surfaces

Journal

Physical Review B, 56(3)

Author

Huff, W.R.A.

Publication Date

1996-11-05

LBNL-39524
UC-410
Preprint

ERNEST ORLANDO LAWRENCE
BERKELEY NATIONAL LABORATORY

A Study of Angle-Resolved Photoemission Extended Fine Structure as Applied to the Ni 3*p*, Cu 3*s*, and Cu 3*p* Core-Levels of the Respective Clean (111) Surfaces

W.R.A. Huff, Y. Chen, S.A. Kellar, E.J. Moler, Z. Hussain, Z.Q. Huang, Y. Zheng, and D.A. Shirley
Accelerator and Fusion Research Division

November 1996
Submitted to
Physical Review B

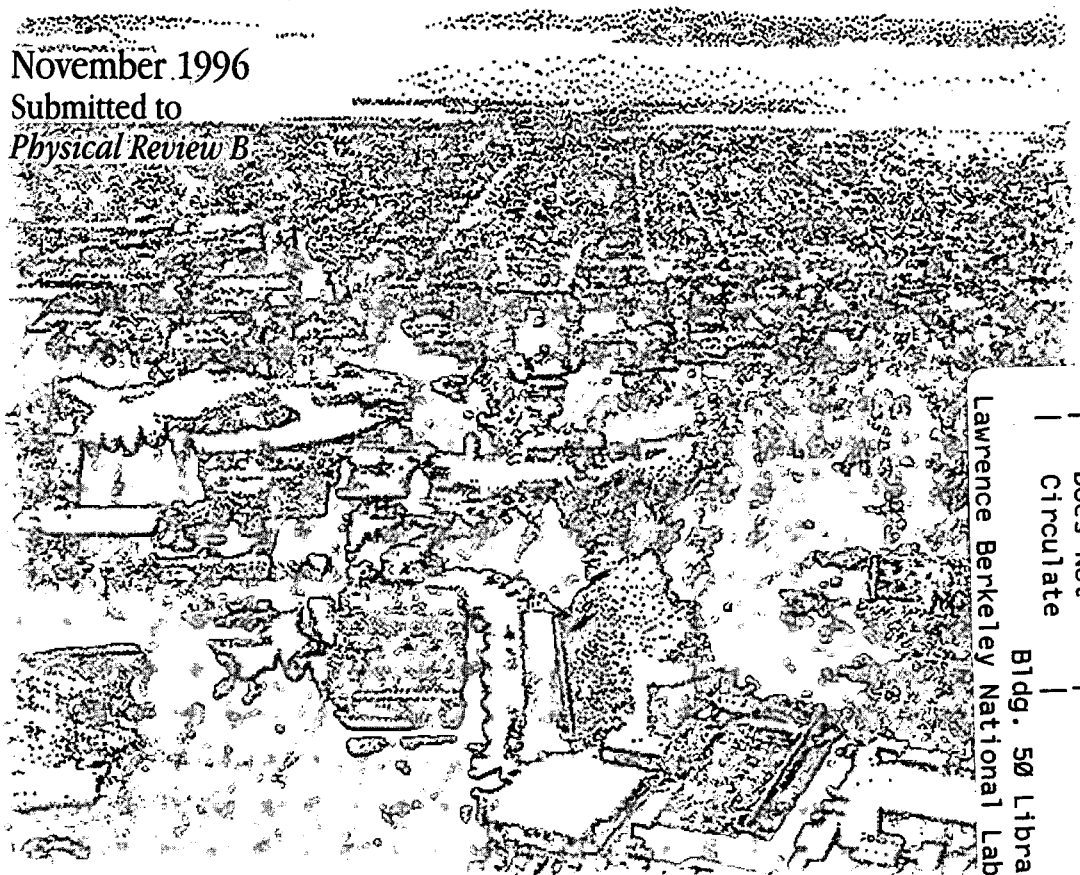

DISCLAIMER

LBNL-39524
LSBL-355
UC-410

A STUDY OF ANGLE-RESOLVED PHOTOEMISSION EXTENDED FINE STRUCTURE AS APPLIED TO THE NI 3*p*, CU 3*s*, AND CU 3*p* CORE-LEVELS OF THE RESPECTIVE CLEAN (111) SURFACES*

W.R.A. Huff [a,b], Y. Chen[c], S.A. Kellar[a,b], E.J. Moler[a,b], Z. Hussain[a], Z.Q. Huang[d], Y. Zheng[e], and D.A. Shirley[c]

[a]Advanced Light Source, Accelerator & Fusion Research Division, Ernest Orlando Lawrence Berkeley National Laboratory, University of California, Berkeley, California 94720
[b]The University of California, Dept. of Chemistry, Berkeley, CA 94720
[c]The Pennsylvania State University, Department of Chemistry and Physics, University Park, PA 16802
[d]Present address: James Franck Institute, Univesity of Chicago, IL 60637
[e]Present address: Oplink, San Jose, CA 95131

*This work was supported by the Director, Office of Energy Research, Office of Basic Energy Sciences, Materials Sciences Division, of the U.S. Department of Energy, under Contract No. DE-AC03-76SF00098.

A Study of Angle-Resolved Photoemission Extended Fine Structure as Applied to the Ni 3*p*, Cu 3*s*, and Cu 3*p* Core-Levels of the Respective Clean (111) Surfaces

W.R.A. Huff,[a,b] Y. Chen,[c] S.A. Kellar,[a,b] E.J. Moler,[a,b]
Z. Hussain,[a] Z.Q. Huang,[d] Y. Zheng,[e] and D.A. Shirley[c]

[a]Lawrence Berkeley National Laboratory, Berkeley, CA 94720

[b]The University of California, Dept. of Chemistry, Berkeley, CA 94720

[c]The Pennsylvania State University, Dept. of Chemistry and Physics, University Park, PA 16802

[d]Present address: James Franck Inst., U. of Chicago, IL 60637

[e]Present address: Oplink, San Jose, CA 95131

ABSTRACT

The first non-*s* initial state angle-resolved photoemission extended fine structure (ARPEFS) study of clean surfaces for the purpose of further understanding the technique is reported. The surface structure sensitivity of ARPEFS applied to clean surfaces and to arbitrary initial states is studied using normal photoemission data taken from the Ni 3*p* core levels of a Ni(111) single crystal and the Cu 3*s* and the Cu 3*p* core-levels of a Cu(111) single crystal. The Fourier transforms of these clean surface data are dominated by backscattering. Unlike the *s* initial state data, the *p* initial state data show a peak in the Fourier transform corresponding to in-plane scattering from the six nearest-neighbors to the emitter. Evidence was seen for single-scattering events from in the same plane as the emitters and double-scattering events.

Using a newly developed, multiple-scattering calculation program, ARPEFS data from clean surfaces and from *p* initial states can be modeled to high precision. Although there are many layers of emitters when measuring photoemission from a clean surface, test calculations show that the ARPEFS signal is dominated by photoemission from atoms in the first two crystal layers. Thus, ARPEFS applied to clean surfaces is sensitive to surface reconstruction. The known contraction of the first two Cu(111) layers is confirmed. The best-fit calculation for clean Ni(111) indicates an expansion of the first two layers.

PACS Number: *61.14.-x, 61.14.Qp, 61.14.Rq, 68.35.Bs, 68.55.Jk*

1. INTRODUCTION

Angle-resolved photoemission extended fine-structure (ARPEFS) is a well established technique for determining surface structures.[1-5] ARPEFS has been used to determine the structures of adsorbate systems as well as molecular adsorbates on conducting single crystal surfaces. ARPEFS yields precise information about both the local structure around the adsorbates, including the adsorbate-induced relaxation of the substrates.[6-12] These studies have shown that ARPEFS data and their Fourier transforms (FTs) can be described mainly in terms of backscattering events. The positions of all the strong peaks in ARPEFS-FTs from adsorbates can be predicted from a trial structure with fairly good accuracy based on a single-scattering cluster model together with the concept of a backscattering cone.

The purpose of this paper is to explore the applicability of ARPEFS to non-*s* initial state photoemission from clean surfaces. The immediate goal is to observe and to understand the phenomenon in a simple, known system. The long-range goal is to develop a method for studying photoemission from arbitrary initial states as well as to determine the atomic structure of interfaces, for which ARPEFS seems ideally suited. In favorable cases, atomic relaxation and reconstruction could be studied as well. In such studies, the elemental and chemical specificity of ARPEFS and its sensitivity to atomic layers that are several layers below the surface would be advantageous.

If the photoelectron signals from surface and bulk atoms are resolvable in ARPEFS studies of clean surfaces, then the data analysis may be based on multiple ARPEFS curves. For the more common case in which signals from different layers cannot be resolved, reconstruction or relaxation effects may still be modeled by fitting the single experimental ARPEFS curve. In the absence of a surface core-

level shift, the ARPEFS curve may or may not be surface sensitive enough to yield a conclusion about a possible surface reconstruction.

Most of the previous ARPEFS studies have been based on photoemission data from atomic *s* core-level initial states, for which the dipole selection rules $\Delta\ell_i = \pm 1$, and $\Delta m_i = 0$ give a p_o-wave final state. Experience with ARPEFS data from non-*s* initial states and their FTs is very limited, however.[13-15] For non-*s* initial states ($\ell_i \neq 0$), partial waves with orbital quantum numbers $\ell_i + 1$ and $\ell_i - 1$ contribute to the photoemission intensity. There is a phase relationship between them which leads to interference between the partial waves. Note that the allowed m levels will be populated in the final state. Thus, with a p initial state, the photoemitted partial waves consist of $\ell_f = 0$, $m_f = m_i = 0$ as well as $\ell_f = 2$, $m_f = m_i = 0, \pm 1$. The partial wave radial dipole matrix elements and the phase shifts are generally energy dependent. It is important to note that the *intensities* from the different m levels are summed, not the amplitudes.[16] The intensities are also summed over the different emitters, e. Thus, for the given partial waves, $\psi_{\ell_f,m}(\theta,\phi,k)$, the total intensity from an isolated atom, $I_{tot}(\theta,\phi,k)$, is

$$I_{tot}(\theta,\phi,k) = \sum_e \sum_m \left| \sum_{\ell_f} (-i)^{\ell_f} R_{\ell_f}(k) e^{i\delta_{\ell_f}(k)} \left\langle Y_{\ell_f,m} \middle| Y_{1,0} \middle| Y_{\ell_i,m} \right\rangle \psi_{\ell_f,m}(\theta,\phi,k) \right|^2 \quad (1)$$

$\left\langle Y_{\ell_f,m} \middle| Y_{1,0} \middle| Y_{\ell_i,m} \right\rangle$ is the overlap integral between the initial and final spherical harmonic wave functions which are functions of θ and ϕ. $R_{\ell_f}(k)$ are the partial wave radial dipole matrix elements and $\delta_{\ell_f}(k)$ are the phase shifts. Despite these complications, there are a number of experimental situations for which ARPEFS from an arbitrary initial state may be the most suitable method of study.

Two different data sets are presented here. The first set is from the 3p core-levels of a clean Ni(111) surface. Due to fitting complications caused by the

satellites (figure 1a), a second ARPEFS data set was taken from the Cu 3*s* and the Cu 3*p* (figure 1b) core-levels of a clean Cu(111) single crystal. These Cu 3*s* and Cu 3p data are used to study the non-*s* initial state photoemission from a clean surface in a carefully controlled manner.

Section 2 discusses the experimental details. Sections 3,4,5 and 6 discuss the data reduction, the Fourier analysis, the multiple-scattering analysis, and the error analysis, respectively. Section 7 provides a discussion which includes a comparison between the nickel data and an adsorbate system as well as some test calculations performed to better understand the scattering processes.

2. EXPERIMENTAL

The data were collected in an ultra-high vacuum chamber (*pressure* $\leq$ 60 nPa) equipped with a rotatable, angle-resolved, hemispherical electron energy analyzer[17] and standard ultra-high vacuum surface science instrumentation. The sample manipulator allows for either liquid nitrogen or liquid helium cooling. The crystals were cleaned by repetitive cycles of Ar^+ sputtering and subsequent annealing by e-beam heating to 700 °C. The sample cleanliness was monitored using synchrotron x-ray photoemission spectroscopy.

The Ni(111) experiment was performed at the National Synchrotron Light Source at Brookhaven National Laboratory on beamline U3-C. The crystal was cooled to $\lesssim$100 K throughout the data collection; no contamination was detected before or after the Ni data collection which lasted 9.5 hours. The light was oriented 55° from the surface normal away from the crystal (011) plane. The photon polarization vector, $\vec{\varepsilon}$, was thus oriented 35° from the surface normal and perpendicular to the crystal (011) plane (see illustration in figure 2). The analyzer

was oriented 4° off-normal from the Ni(111). The total experimental energy resolution was ~3.0 eV.

The Cu(111) experiments were performed using the Advanced Light Source at the E. O. Lawrence Berkeley National Laboratory on beamline 9.3.2.[18] The crystal was cooled to ~80 K throughout the data collection, which lasted five hours for each ARPEFS curve. The photon polarization vector, $\vec{\varepsilon}$, was oriented 10° from the surface normal (see illustration in figure 3). The analyzer was oriented 5° from the surface normal.

The raw ARPEFS data are a series of x-ray photoemission spectra, each with a different kinetic energy. The magnitude of the photoelectron wave vector ranged from 5.1 - 10.5 $Å^{-1}$ for the nickel data and 5.0 - 11.9 $Å^{-1}$ for both copper data sets. All of the spectra were recorded in equal 0.1 $Å^{-1}$ steps.

3. DATA REDUCTION

Each peak was fit with a a Voigt function added to a step-function with a step-height scaled to the respective peak intensity and a step-width taken as the Gaussian width of the peak. This step-function models the inelastic scattering background of the photoemission spectrum. The total fit is the solid line through the data points in figures 1a and 1b.

The purpose of fitting the spectra is to extract the most accurate area from the peaks, reducing the data to the $\chi(k)$ diffraction curve which contains the structural information. $\chi(k)$ is defined by[19]

$$\chi(k) = \frac{I(k)}{I_0(k)} - 1 \qquad (2)$$

where $I(k)$ is the peak area plotted as a function of the peak position in k.. $I_0(k)$ is a smooth, slowly varying function with an oscillation frequency much lower than $I(k)$; $I_0(k)$ stems from the contribution of the inelastic background and the atomic cross section. It is adequate to use a simple spline function to fit $I_0(k)$.[20]

Removing $I_0(k)$ results in a suppression of the FT the peaks $\lesssim 2$ Å. In photoemission from clean surfaces, many forward scattering path-length differences from sub-surface emitters will be $\lesssim 2$ Å. This forward scattering signal is therefore removed during the data reduction along with the $I_0(k)$. The extracted experimental ARPEFS $\chi(k)$ curve is thus dominated by backscattering.

Figure 2 plots the Ni $3p$ experimental $\chi(k)$ curve (solid line) which represents the sum of the Ni $3p_{3/2}$ and Ni $3p_{1/2}$ areas shown in figure 1a. The best-fit result from the multiple-scattering modeling calculations is also shown in figure 2 (dashed line) and will be discussed in section III.B.1.

Figure 3 overlays the Cu $3s$ and the Cu $3p$ ARPEFS $\chi(k)$ curves. The experimental geometry is also shown. The data are plotted in this way to clearly illustrate that the ARPEFS data from an s atomic core-level are ~180° out of phase from ARPEFS data from a p atomic core-level. This result is expected and has been studied previously.[13-15]

4. Fourier Analysis

It is useful to study the auto-regressive linear prediction based Fourier transform (ARLP-FT) to transform from momentum space to real space.[2, 5, 6, 21] In ARPEFS, the positions of the strong peaks in ARLP-FTs from adsorbate/substrate systems can be predicted with fairly good accuracy using the single-scattering cluster model together with the concept of strong backscattering from atoms located within a cone around 180° from the emission direction. The effective solid

angle of this backscattering cone is ~30° - 60°; it is not unique, but is operationally defined simply by opening the angle until it can account for the observed FT peaks based on the crystal geometry. Signals from scattering atoms very close to the source atom may be observable, even if the scatterers lie outside the nominal backscattering cone.

The FT peaks correspond to path-length differences (PLDs), ΔR_j, between the component of the photoelectron wave that propagates directly to the detector and the components which are first scattered by the atomic potentials within this backscattering cone.[6] Thus, the peak positions are approximately

$$\Delta R_j = r_j\left(1-\cos\theta_j\right) \tag{3}$$

where r_j is the bond length from the emitter to a given atom, j, and θ_j is the scattering angle (180° for exact backscattering). Note that the effect of the atomic scattering phase shift is ignored in this approximation. The scattering takes place inside the crystal and the ARPEFS data must be shifted from the measured $\chi\left(k_{\text{outside-crystal}}\right)$ to $\chi\left(k_{\text{inside-crystal}}\right)$ to account for the inner potential. In ARPEFS modeling calculations, the inner potential is treated as an adjustable parameter and is typically 5 - 15 eV. The inner potential is approximately the sum of the work function and the valence band-width.[22] Thus, before Fourier transformation, the ARPEFS data presented here were shifted by 10 eV to higher kinetic energy.

4.1. Ni(111)

The ARLP-FT of the Ni 3*p* experimental ARPEFS data is plotted in figure 4a. Also illustrated in figure 4 is a schematic of a [111] single crystal, assuming a bulk-terminated fcc surface, with a backscattering cone superimposed. The FT

shows peaks due to scattering from atoms up to four layers below the emitting atoms. The depth sensitivity of ARPEFS has been described previously and was found to be enhanced by multiple-scattering effects.[5]

The atoms and corresponding peaks are labeled in figure 4. Using the bulk nickel nearest-neighbor spacing, 2.49 Å, the expected peak positions can be calculated using simple geometry. These expected peak positions along with the experimental peak positions and their corresponding shifts are listed in table 1. Table 1 also lists an assignment of each peak to single-scattering (SS) or double-scattering (DS) events. Additionally, the number of atoms contributing to each peak is listed in table 1.

The origins of the peaks labeled 2, 3, 4, 5, and 6 are straightforward. If a line is drawn from a surface emitter into the crystal and normal to the (111) plane, peaks 2, 3, and 6 occur due to single-scattering from the three atoms closest to this line in layers 2, 3, and 5, respectively. Nickel has an fcc crystal structure and thus peak 4 is due to direct backscattering (θ_j=180°) from the #4 atom which is in layer 4. Peak 5 is due to single-scattering from the #5 atoms which are the six nearest neighbors to atom #4.

Peaks 2' and 3' may be attributed to atoms more laterally distant from the line described above. Peak 2' occurs due to single-scattering from the three second nearest-neighbors to this line in layer 2. Similarly, peak 3' occurs due to single-scattering from the three second nearest-neighbors to this line in layer 3.

Double-scattering may be detectable in the ARLP-FT as evidenced by peaks 2*, 3*, 4*, and 5*. The first event for peak 2*, for example, is scattering by the #2 atoms. The second event is scattering by the #2 atoms' six nearest neighbors. Given that there are three #2 atoms, eighteen atoms are available for the second scattering event to give peak 2*. An analogous process holds for the 3* peak. Because there is only one #4 atom for each emitter in the fcc ($\dot{a}bc\dot{a}bc$) geometry,

only six atoms are in position for the second scattering event to give peak 4*. However, there are six #5 atoms and thus thirty-six atoms for the second scattering event to give peak 5*.

These assignments due to double-scattering are somewhat speculative. It is believed that peaks 4* and 5* have a higher relative amplitude as compared to 2* and 3* because waves scattering in the fourth layer can be forward-focused by atoms in the surface layer. Also, the higher probability for the second scattering event of peak 5* due to the greater number of atomic potentials will increase its relative amplitude.

A new result is also noted in this ARLP-FT. The peak labeled 1 is due to in-plane scattering of the photoemission wave from the six nearest-neighbors to the emitter. In-plane scattering for normal emission has not been observed previously for *s* initial state data or calculations. In *s* initial state photoemission, the outgoing p_o wave destructively interferes with itself for θ_j=90° due to the negative parity of a *p*-wave. In *p* initial state photoemission, however, the photoemitted *d* and *s* waves which are interfering with themselves and with each other have positive parity and do not cancel for normal emission, in-plane scattering. Thus, the frequency component labeled peak 1 is a physical part of the $\chi(k)$ diffraction curve and the appropriate PLD peak is observed. A peak that would be labeled 1' arising from in-plane scattering by the second nearest-neighbors would be seen at ~4.31 Å. If present, this weak feature is obscured by peak 2.

4.2. Cu(111)

Figure 4b plots the ARLP-FT of the Cu 3*s* and the Cu 3*p* ARPEFS data. The interpretation of each FT peak is similar to the Ni FT discussion above. Cu(111) is also fcc and the bulk nearest-neighbor spacing is 2.56 Å.

The expected peak positions are listed in table 2 along with the experimental peak positions and corresponding shifts for the Cu 3*s* and Cu 3*p* data FTs. Table 2 also lists an assignment of each peak to single-scattering (SS) or double-scattering (DS) events. Additionally, the number of atomic scattering potentials contributing to each peak is listed in table 2.

From the single-scattering values listed in table 2, one can see that the structure can generally be determined to ±0.5 Å by simply analyzing the ARLP-FT. Given this precision, some peaks seem to correlate with double-scattering PLDs. Again, these assignments due to double-scattering events are somewhat speculative. To be certain that these small features are not artifacts caused by the finite data range, one must study the FT in more detail than has been done to date. Additionally, one must better understand any slight shifting of the peaks resulting from mathematically extending the data range using the ARLP method.

An interesting feature of the Cu 3*s* FT as compared to the Cu 3*p* FT is the intensity differences between some of the peaks. If the ARPEFS data from these different initial states were identical but out of phase, then their respective peak positions and intensities would be identical. These data are more than simply out of phase. Peak 1 in the Cu 3*p* FT is not present in the Cu 3*s* FT. The origin of peak 1 is analogous to peak 1 in the Ni 3p FT.

5. Multiple-Scattering Analysis

Calculations were performed to model the ARPEFS $\chi(k)$ curves. Modeling calculations are very useful because, in addition to allowing a precise structure determination, a variety of test cases can be used to better understand the scattering processes. Using the single-scattering model of ARPEFS,[6, 19] $\chi(k)$ is written as

$$\chi(k) = \sum_j A_j(k) \cos\left[k\left(R_j - R_j \cos\theta_j\right) + \phi(k)\right] \tag{4}$$

where $A_j(k)$ contains experimental geometry factors including the photon polarization direction and the electron emission direction as well as the scattering amplitude, angle integration, and thermal averaging. $\phi(k)$ is the atomic scattering phase-shift.

At $\theta_j = 0°$, there is zero path-length difference (PLD) between the direct and scattered photoelectron waves. For forward-scattering through angles close to 0°, the scattering amplitude is quite large, but many path-length differences are correspondingly small and do not show up in the FTs.

The multiple-scattering spherical-wave (MSSW) code developed by Barton *et al.*[6, 19, 20, 23] has been proven to precisely model s initial state core-level photoemission.[6-11] However, the ARPEFS data and FTs from a p initial state require both s and d partial waves to describe the photoemission signal. Kaduwela and Fadley[24] developed a code based on the Rehr-Albers formalism[25] which has been discussed and applied to photoelectron diffraction from arbitrary initial states by Friedman and Fadley.[26] A new code developed by Chen, Wu, and Shirley[27] which is also based on the Rehr-Albers formalism[25] was used for the calculations presented here. Due to the summing methods used in this new code, it is significantly faster than the previous codes. Thus, fitting calculations can be performed for systems in which the photoemitters are in many layers and the core-level initial state has arbitrary angular momentum.

For the Ni $3p$ and the Cu $3p$ calculations, the radial dipole matrix elements, $R_{\ell_i \pm 1}$, and phase shifts, $\delta_{\ell_i \pm 1}$, were those calculated by Goldberg, Fadley, and Kono[28, 29]. These inputs to the scattering calculation describe the amplitude and phase relationship between the photoelectron partial waves, $\ell_i \pm 1$, as a function of

the photoelectron kinetic energy. The atomic-scattering phase shifts were calculated using the atomic potentials tabulated by Moruzzi *et al.*[30]

To account for vibration effects of the bulk atoms, the mean square relative displacement (MSRD) was calculated using equation (33) by Sagurton *et al.*[4]

$$\left\langle u_i^2 \right\rangle \propto \frac{1}{M_i \theta_{\mathrm{D},i}} \left(1 + \frac{cT^2}{\theta_{\mathrm{D},i}^2} \cdots \right) \tag{5}$$

M_i is the atomic mass, $\theta_{\mathrm{D},i}$ is the correlated Debye temperature, T is the sample temperature, and c is a coefficient that varies slowly with temperature. For calculating the MSRD of the bulk Ni (Cu) atoms, $\theta_{\mathrm{D},i}$ was 450 K (350 K) and T was 80 K. The effects of the surface atom vibrations on photoelectron diffraction data has been discussed previously.[12, 31]

The surface sensitivity of ARPEFS in the study of clean surfaces is strongly dependent on the inelastic mean free path (IMFP). The IMFP calculation is important to high-precision modeling of such data. Certainly, many emitters lie several layers below the surface region and their signal never escapes the crystal. The IMFP was included using the exponential damping factor $e^{-r/\lambda}$ where λ was calculated using the Tanuma, Powell, and Penn (TPP-2) formula.[32]

Figure 2 plots the best fit (dashed line) overlaying the experimental ARPEFS data (solid line) for the Ni(111) 3p data. A 74 atom cluster was used for the MSSW calculation. The emission angle was allow to vary and found to be 4° off-normal with an inner potential of 7.4 eV. Because the experimental Ni 3*p* ARPEFS amplitude was unusually low, it was scaled by a factor of five to be consistent with the calculated amplitude. This scaling does not affect the results because the relative amplitudes and the oscillation frequencies are preserved. The

spacing between the first two nickel layers was determined to be 2.09(1) Å which is a 3% expansion of the bulk value, 2.03 Å.

Figure 5a overlays the experimental Cu 3*s* ARPEFS data (solid line) with its best fit (dashed line). Figure 5b overlays the experimental Cu 3*p* ARPEFS data (solid line) with its best fit (dashed line). For each fit, a 74 atom cluster was used. The emission direction was found to be 5° off-normal. Due to its unusually strong affect on the fit quality, the inner potential was fixed at 10 eV as discussed above. The modeling calculations determined that $d_{1,2}$ = 2.06(5) Å which is a 1.5% contraction from the bulk value, 2.09 Å. Within the error bars of our experiment, this result is consistent with previous LEED studies which found a contraction of 0.7(5) %.[33, 34]

6. Error Analysis

The best fit is determined by an *R*-factor minimization.[27, 35] The parameters with the largest effect on the *R*-factor were the spacing between the first two crystal layers and the photoemission angle. Figure 6 plots the *R*-factor for the Ni 3*p* fitting as the Ni_1-Ni_2 interlayer spacing is varied.

The *R*-factor as a function of the emission angle as measured from the surface normal, θ_e, and the azimuthal angle about the surface normal, ϕ_e, was minimized for both Cu data sets. These contour plots are illustrated in figures 7a and 7b for the Cu 3*s* and Cu 3*p* fitting calculations, respectively. The sample's orientation with respect to the photon beam, and thus the photon polarization vector, was maintained constant. θ_e was varied from 0° to +10° stepping by 1° and ϕ_e was varied from 0° to 180° stepping by 10°. The fcc surface is six-fold symmetric but the bulk is three-fold symmetric. The surface atoms are in the fcc

three-fold hollow site and $\phi_e = 0°$ was chosen to bisect one edge of the equilateral triangle formed by this three-fold hollow site, the [100] direction. Thus, a mirror plane exists and these R-factor calculations were symmetrized to obtain the results for $\phi_e = 180°$ to $360°$.

Comparing figures 7a and 7b shows some very interesting differences between the Cu $3s$ and the Cu $3p$ ARPEFS data. From figure 7a (the Cu $3s$ contour plot), the R-factor minimum is at $\theta_e = 4.5° \pm 1°$. The minimum is very shallow toward normal emission ($\theta_e = 0°$) but becomes steep more off-normal ($\theta_e > 5°$). Figure 7b (the Cu $3p$ contour plot) is markedly different due to final-state effects. The R-factor minimum is $\theta_e = 5.5° \pm 0.5°$ is very steep both toward and away from normal emission ($\theta_e < 5°, \theta_e > 6°$). For the Cu $3p$ data, the $\theta_e = 0°$ fit was very poor while the $\theta_e = 5°$ fit was quite good. These results have significant implications with respect to modeling ARPEFS data from non-s initial states.

The R-factor also changes as a function of ϕ_e due to final-state effects. For both the $3s$ and the $3p$ initial states, the R-factor is not sensitive to changing ϕ_e if θ_e is near normal emission ($\theta_e < 5°$). Even at the minimum ($\theta_e \approx 5°$), the R-factor remains rather insensitive to changing ϕ_e. However, for the $3p$ initial state, the three-fold symmetry of the adsorption site begins to become evident. As θ_e is increased even more ($\theta_e > 5°$), the R-factor varies significantly with changing ϕ_e and the three-fold symmetry of the adsorption site is evident in both contour plots. This effect is due to backscattering. As the emission angle becomes more off-normal, backscattering from the second-layer Cu atoms is enhanced in the ARPEFS $\chi(k)$ curve.

These results from θ_e and ϕ_e indicate that the detected intensity distribution of Cu $3s$ photoemission is less directional than the detected intensity distribution of Cu $3p$ photoemission. As discussed previously, photoemission data from atomic s

core-level initial states gives a p_o-wave final state. Thus, the intensity distribution from the Cu $3p$ core-level initial states must have mostly d-wave character.

It should be noted that the calculations can be symmetrized as described above because the photon polarization vector is normal to the surface. Experience with fitting ARPEFS data suggests that the oscillation frequencies of the $\chi(k)$ curve are rather insensitive to the photon polarization vector orientation. However, the relative oscillation amplitudes are dependent on this orientation. These amplitude variations will change the magnitude of the R-factor and perhaps break this three-fold symmetry. Thus, if the photon polarization vector is significantly off-normal, then ϕ_e should be calculated from 0° to 360°.

7. DISCUSSION

Figure 8 compares the Ni $3p$ data with $\left(\sqrt{3}\times\sqrt{3}\right)R30°$Cl/Ni(111) data published previously.[36] This comparison illustrates the similarities and differences between adsorbate systems and clean surfaces as well as between s and p core-level initial state ARPEFS data. As expected, the Cl $1s$ data and the Ni $3p$ data are roughly 180° out of phase.

Also, the FTs are remarkably similar, with ARLP-FT peaks for backscattering from layers below the source atom being resolved in both cases. The FT shows the slight lattice spacing difference between the two surfaces. Additionally, the Ni $3p$ FT show a peak at ~2.5 Å due to effects described in section III.A.1 whereas the Cl $1s$ FT has no such peak.

The similarity of the two ARLP-FT spectra shows that ARPEFS of a clean crystal is dominated by backscattering. The ARPEFS intensity can be regarded as arising from the sum of contributions from emitting atoms in each layer. If we neglect forward scattering from atoms in layers above the source atoms, the ARPEFS intensity is due to backscattering from the atoms in layers below the

source atoms. Due to the finite mean free path, the signal from the sub-surface layer atoms is damped.

Using the best-fit parameters for the Cu(111) 3*s* and 3*p* data, some test calculations were completed to study the scattering in more detail. The test cluster was a single emitter positioned 2.06 Å above a layer of scattering atomic potentials. The distance and geometry were chosen such that the layer simulated the second layer of the fcc Cu(111). In addition to testing for double-scattering, this test allows for the simulation of the intensity differences between the Cu 3*s* and Cu 3*p* FTs in figure 4b. Note that the ARLP method was not applied to these test $\chi(k)$ curves because they were calculated directly over a wide *k*-range (4 - 20 $Å^{-1}$).

This geometry should give rise to peaks at PLDs correlating with the 2 and 2' positions for single-scattering and the 2, 2', and 2* positions for double-scattering. Figure 9a plots the Cu 3*s* FT for a single-scattering calculation (solid line) and a double-scattering calculation (dashed line). Figure 9b plots the Cu 3*p* FT for a single-scattering calculation (solid line) and a double-scattering calculation (dashed line). The insets show the respective $\chi(k)$ curves which were filtered to pass only those PLDs > 3.5 Å which removes some low frequency oscillations unrelated to PLDs. The 2* peak distinctly appears in the Cu 3*p* FT even though there are only minor differences in the $\chi(k)$ curves. The 2* peak is not as convincing in the Cu 3*s* FT.

A striking difference between the Cu 3*s* and Cu 3*p* FTs is the occurrence of peaks 2" and 2"' in only the Cu 3*s* FT. Each additional prime represents scattering from the next laterally distant atomic potential. This difference is also observed in the ARLP-FT of the ARPEFS data for the peak $\lesssim$7 Å and is the reason for the chosen 2* position in figure 4b. These results again indicate that Cu 3*p* photoemission intensity is more directional than the Cu 3*s* photoemission intensity.

For the study of clean surfaces or multilayers, it is important to understand the contribution of emitters in sub-surface layers to the overall $\chi(k)$ data. This test used a ten layer fcc Cu(111) cluster with a single emitter. This emitter was subsequently moved from the surface to each layer, ending with the sixth. The cluster was constructed such that the photoemitted wave from the emitter in the sixth layer was subject to the same backscattering environment as the photoemitted wave from the emitter in the surface layer. This is true to four layers below the emitter which is the cut-off seen in the ARLP-FT of the ARPEFS data.

Figure 10 shows the multiple-scattering calculation results for this test cluster. The calculation parameters were fixed at the best-fit values discussed previously. The normalized intensity at the detector is plotted as a function of the magnitude of the photoelectron wave vector. The first point to note about these results is that the signal from the Cu 3*s* initial state is a factor of 100 stronger than the signal from the Cu 3*p* initial state. This factor drops out in equation (2) and is thus not seen in the data $\chi(k)$ curves. The reasons for this intensity difference are currently being studied. The next point to note is that the signal drops off drastically between placing the emitter in the second layer and placing the emitter in the third layer. The signal increases slightly when placing the emitter in the fourth layer due to forward-focusing by the surface layer atoms.

When the emitter is placed from the third layer to the sixth layer, the high-frequency oscillations important to ARPEFS become small and the $I(k)$ curves become dominated by the low-frequency oscillations (short path-length differences). This indicates that the signal becomes dominated by forward scattering.

The bottom panel in figure 10 plots $I_{\text{total}}(k)$ which is the sum of the six calculated $I(k)$ curves. This curve simulates the total intensity that would be collected. The low-frequency oscillations are removed by equation (3) when $I(k)$

is divided by a simple spline function to fit $I_0(k)$. The forward scattering signal is therefore removed during the data reduction along with the standard $I_0(k)$. The resulting experimental ARPEFS $\chi(k)$ curve is thus dominated by backscattering. Although the signal from the deeper layers may modulate the high-frequency oscillation magnitudes slightly, the signal is principally due to photoemission from the first two crystal layers. Scattering from six or seven layers is therefore adequate to simulate ARPEFS data.

8. CONCLUSION

To better understand the ARPEFS technique, we studied *s* and non-*s* initial state photoemission from clean metal surfaces. As expected, the Cu 3*s* $\chi(k)$ curve is roughly 180° out of phase from the Cu 3*p* $\chi(k)$ curve. The clean surface ARPEFS data resemble data for adsorbate systems, showing strong backscattering signals from atoms up to four layers below the source atoms. In addition to the backscattering, the Ni 3*p* data and Cu 3*p* data show a peak in the FT at ~2.5 Å corresponding to in-plane single-scattering of the photoemission wave

Although there were many layers of emitters in this clean surface study, the ARPEFS fitting process was sensitive to the surface relaxation. The spacing between the first two nickel layers is 2.09(1) Å which is a 3% expansion from the bulk nickel value. By contrast, the spacing between the first two copper layers is 2.06(5) Å which is a 1.5% contraction from the bulk copper value.

For the Cu(111) 3*s* and 3*p* fitting, the *R*-factor was minimized as a function of ϕ_e and θ_e. These contour plots illustrate that the Cu 3*p* photoemission intensity is more directional than the Cu 3*s* photoemission intensity. This in turn indicates that the photoemission intensity from the Cu 3*p* core-levels must have mostly *d*-wave character.

To study the scattering processes in more detail, two types of test calculations were completed. A cluster with a single emitter adsorbed on a layer of scattering potentials was used to investigate the possibility of detecting double-scattering events directly in the FT. To this end, the Cu 3*p* test results were more convincing than the Cu 3*s* test results. A second test system used a ten-layer cluster and a single emitter moved successively through the first six layers. Although the signal from the deeper layers may modulate the high-frequency oscillation magnitudes slightly, the photoemission signal comes principally from the first two crystal layers.

It has been shown that photoelectron holography signals from clean surfaces are dominated by forward scattering, with atomic positions being imaged up to three layers *ahead* of the emitting atom.[37] A combination of these two photoelectron diffraction techniques would therefore provide a very good method for studying ordered interfaces.

ACKNOWLEDGMENTS

Much appreciation is expressed to Ajith Kaduwela and Chuck Fadley for helpful discussions regarding PEH and their scattering code. This work was supported by the Director, Office of Energy Research, Office of Basic Energy Sciences of the U.S. Department of Energy under Contract No. DE-AC03-76SF00098. The nickel data were collected at the National Synchrotron Light Source at Brookhaven National Laboratory. The copper data were collected with the assistance of the personnel at the Advanced Light Source at the E. O. Lawrence Berkeley National Laboratory.

TABLES

- Table 1: Scattering paths with the calculated PLDs for Ni(111) (based on 2.49 Å nearest neighbor spacing) along with the experimental peak positions and the respective shifts. Layer 1 is defined as the same layer as the emitter. Refer to figure 4 for an illustration of the atomic positions. SS indicates single-scattering and DS indicates double-scattering.

- Table 2: Scattering paths with the calculated PLDs for Cu(111) (based on 2.56 Å nearest neighbor spacing) along with the experimental peak positions and the respective shifts. Refer to figure 4 for an illustration of the atomic positions.

Scattering paths with the calculated PLDs for Ni(111)

Peak Number	Geometric PLD (Å)	Peak Position (Å)	Peak Shift (Å)	Scattering Process	# of Atoms
1	2.49	2.36	-0.13	SS	6
2	4.52	4.69	0.17	SS	3
2'	5.55	5.99	0.44	SS	3
2*	7.01	7.60	0.59	DS	3 × 6
3	8.37	8.45	0.08	SS	3
3'	9.04	9.07	0.03	SS	3
3*	10.86	10.18	-0.68	DS	3 × 6
4	12.18	12.51	0.33	SS	1
5	12.67	12.90	0.23	SS	6
4*	14.67	14.68	0.01	DS	1 × 6
5*	15.16	15.09	-0.07	DS	6 × 6
6	16.37	16.00	-0.37	SS	3

Table 1

Scattering paths with the calculated PLDs for Cu(111)

Peak Number	Geometric PLD (Å)	Cu 3*s* Position (Å)	Cu 3*s* Shift (Å)	Cu 3*p* Position (Å)	Cu 3*p* Shift (Å)	Scattering Process	# of Atoms
1	2.56	---	---	2.39	0.17	SS	6
2	4.65	4.15	-0.50	4.85	+0.20	SS	3
2'	5.71	6.19	+0.48	6.26	+0.55	SS	3
2*	7.21	7.67	+0.46	7.58	+0.37	DS	3 × 6
3	8.61	8.36	-0.25	8.29	-0.32	SS	3
3'	9.30	8.91	-0.39	9.37	+0.07	SS	3
3*	11.17	10.91	-0.26	10.97	-0.20	DS	3 × 6
4	12.54	12.10	-0.44	12.46	-0.08	SS	1
5	13.04	13.20	+0.16	13.12	+0.08	SS	6
4*	15.10	14.96	-0.14	15.13	+0.03	DS	1 × 6
5*	15.60	15.77	+0.17	15.80	+0.20	DS	6 × 6
6	16.85	16.68	-0.17	16.99	+0.14	SS	3

Table 2

FIGURES

- Figure 1: Example photoemission spectrum showing the a) Ni(1$\bar{1}$1) 3*p* data and b) the Cu 3*p* data as well as the Voigt functions and the step functions used to fit the data.

- Figure 2: Ni(111) 3*p* ARPEFS $\chi(k)$ data (solid line) and best fit (dashed line). A schematic of the experimental geometry is shown.

- Figure 3: Comparison of the Cu(111) 3*s* (solid line) and 3*p* (dashed line) ARPEFS $\chi(k)$ data . A schematic of the experimental geometry is shown.

- Figure 4: ARLP based FT of a) the Ni 3*p* and b) the Cu 3*s* (solid line) and Cu 3*p* (dashed line) ARPEFS data. A model of the lattice with the backscattering cone indicates the scattering atoms corresponding to the FT peaks.

- Figure 5: ARPEFS $\chi(k)$ data (solid line) and the MSSW best fit (dashed line) for a) Cu(111) 3*s* and b) Cu(111) 3*p*.

- Figure 6: Ni 3*p* *R*-factor variation with the Ni_1-Ni_2 interlayer spacing.

- Figure 7: a) Contour plot showing how the *R*-factor varies with ϕ_e and θ_e for a) the Cu 3*s* and b) the Cu 3*p* modeling.

- Figure 8: The top panel overlays the $\left(\sqrt{3}\times\sqrt{3}\right)R30°$Cl/Ni(111) (dashed line) with the Ni 3*p* (solid line) experimental ARPEFS curves. The bottom panel overlays their respective ARLP-based FTs.

- Figure 9: FT of the calculated ARPEFS $\chi(k)$ curves (insets) for a) Cu 3*s* and b) Cu 3*p* where a single emitter was adsorbed 2.06 Å above a layer of scattering potentials for single-scattering (solid line) and double-scattering (dashed line).

- Figure 10: The calculated ARPEFS $I(k)$ curves for Cu 3*s* (solid line) and Cu 3*p* (dashed line) where a single emitter was moved successively to deeper layers.

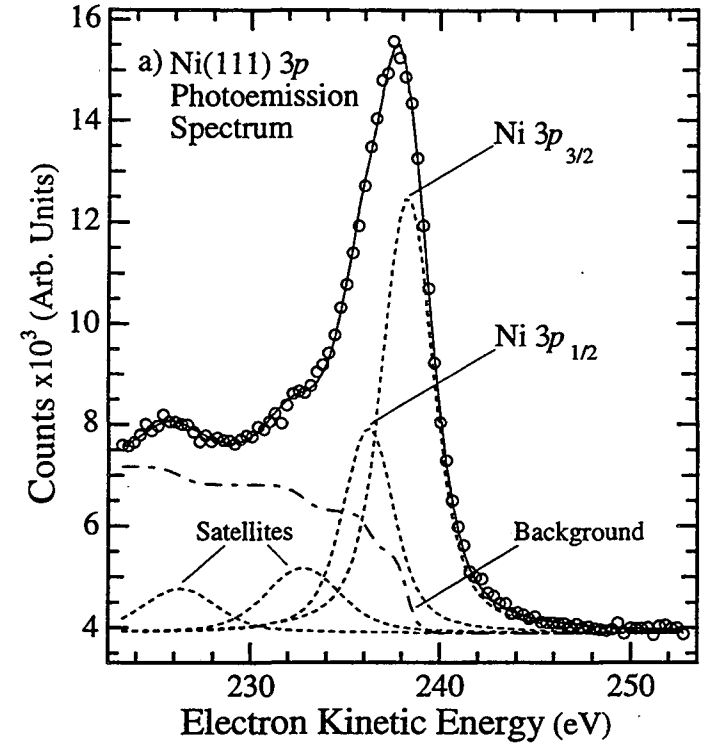

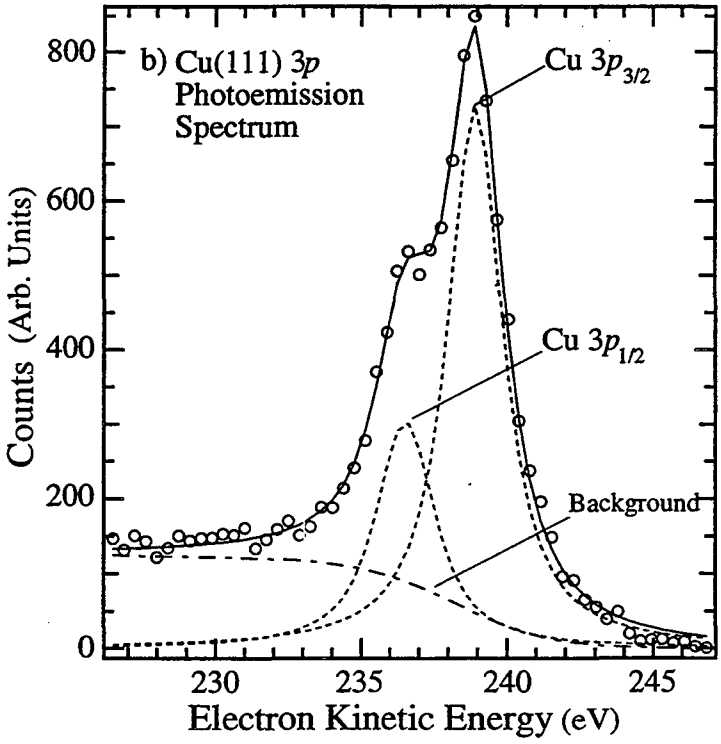

Figures 1a and 1b

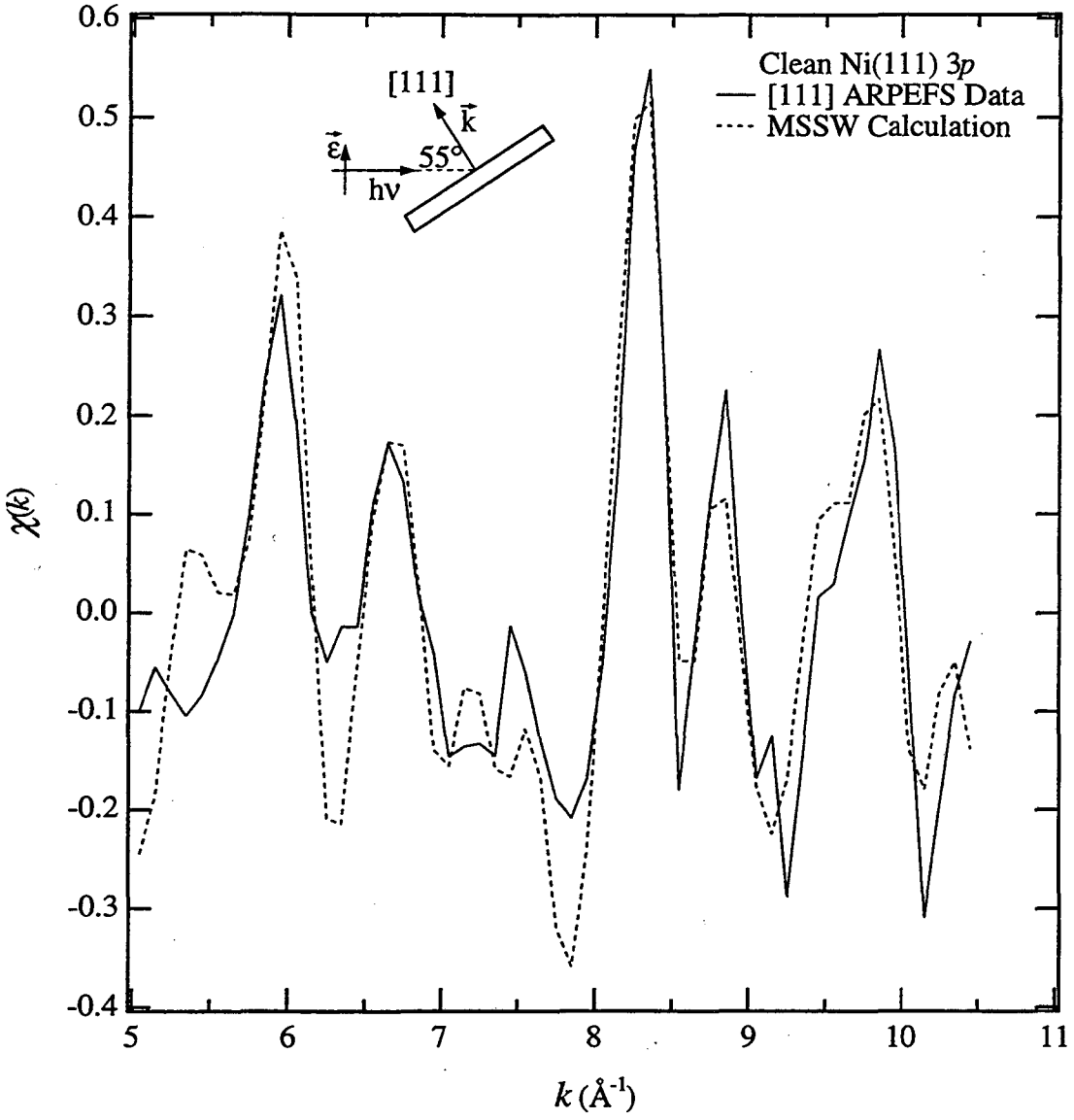
Clean Ni(111) 3p
[111] ARPEFS Data
MSSW Calculation
[111]
k
ε
55°
hν
χ(k)
k (Å-1)
0.6
0.5
0.4
0.3
0.2
0.1
0.0
-0.1
-0.2
-0.3
-0.4
5
6
7
8
9
10
11

Figure 2

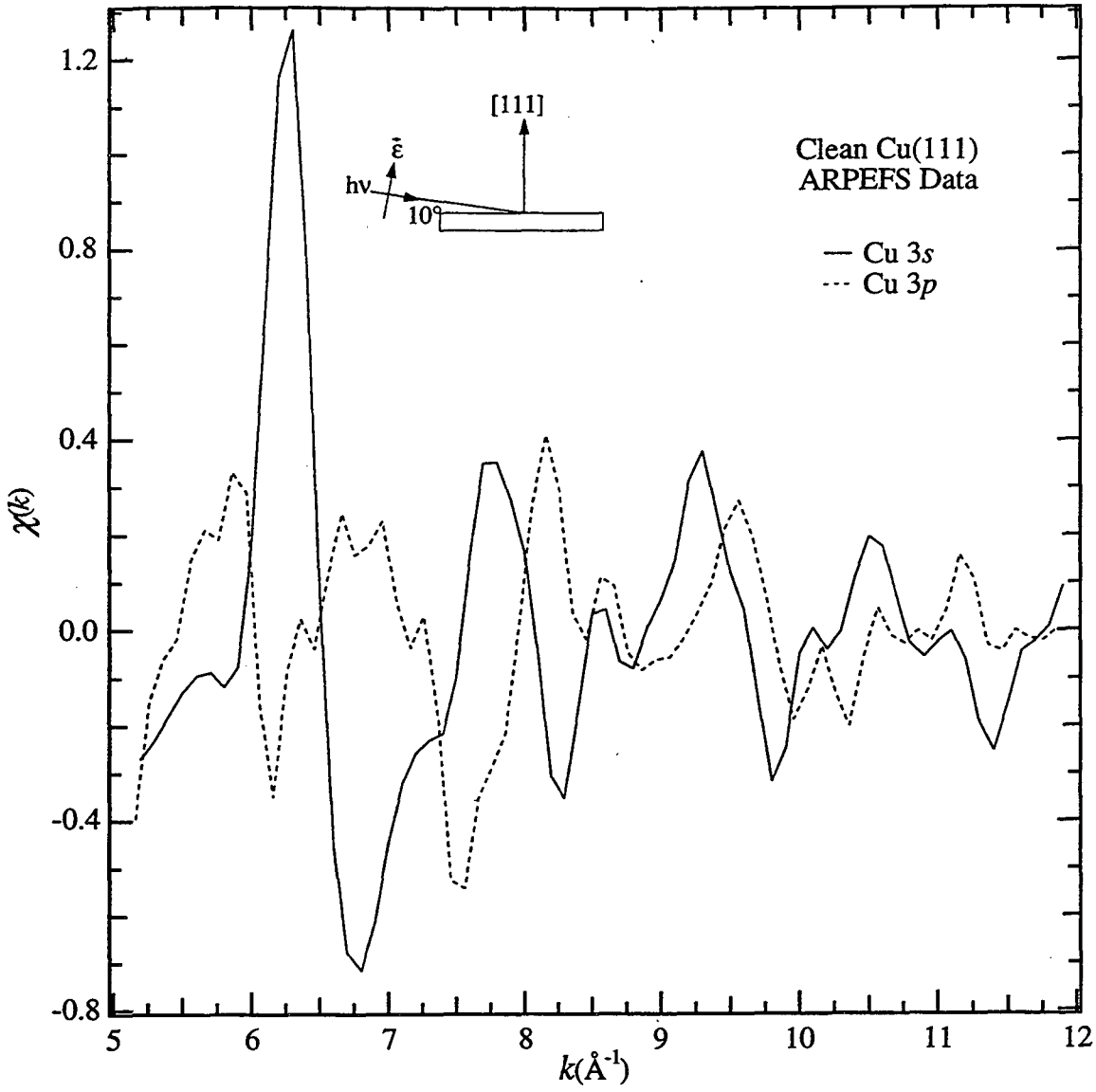
1.2
0.8
0.4
0.0
-0.4
-0.8
χ(k)
5
6
7
8
9
10
11
12
k(Å-1)
[111]
ε̃
hν
10°
Clean Cu(111)
ARPEFS Data
— Cu 3s
--- Cu 3p

Figure 3

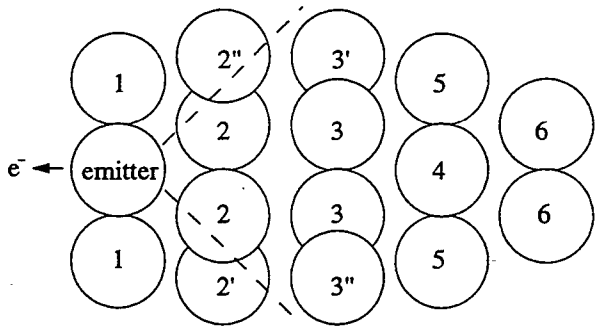

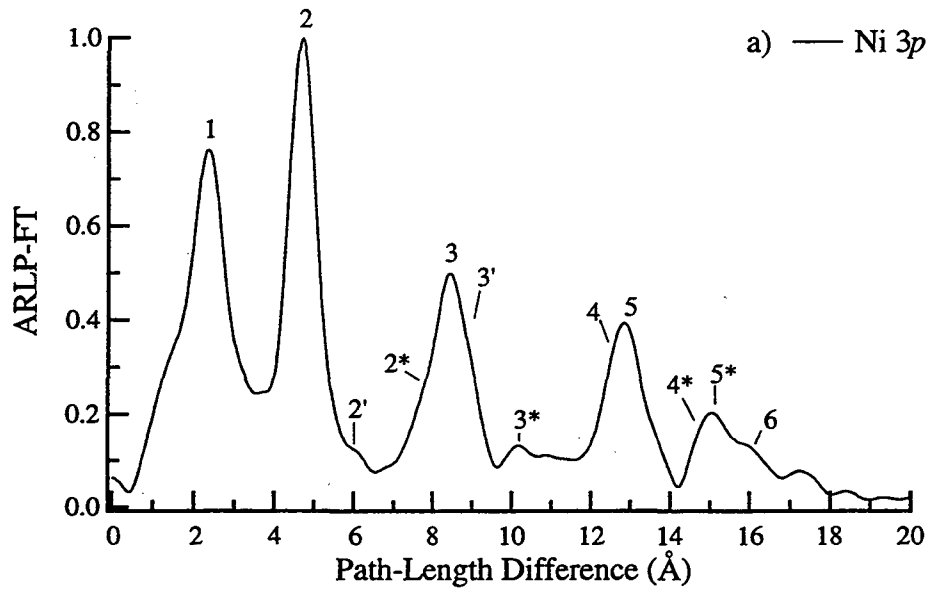

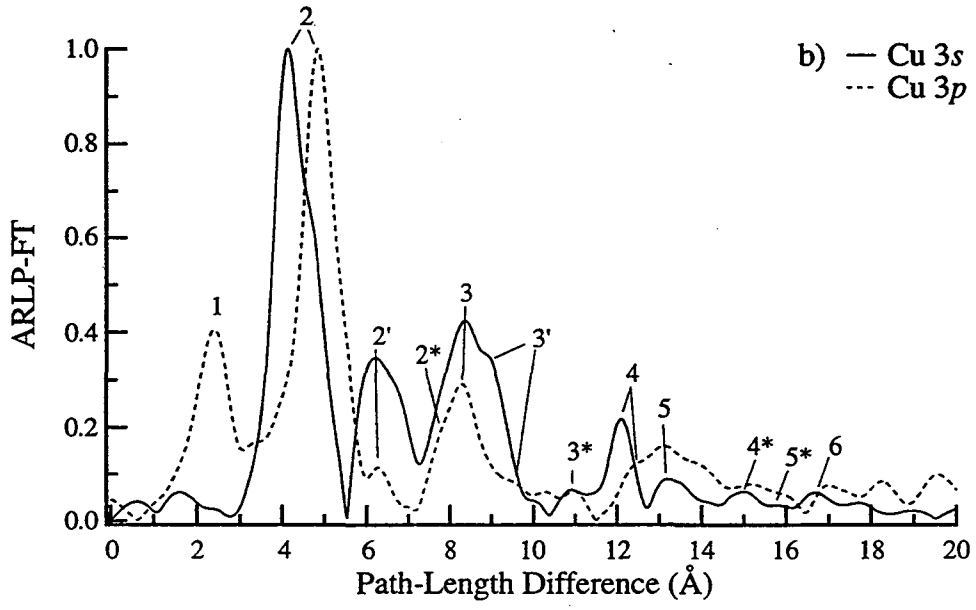

Figures 4a and 4b

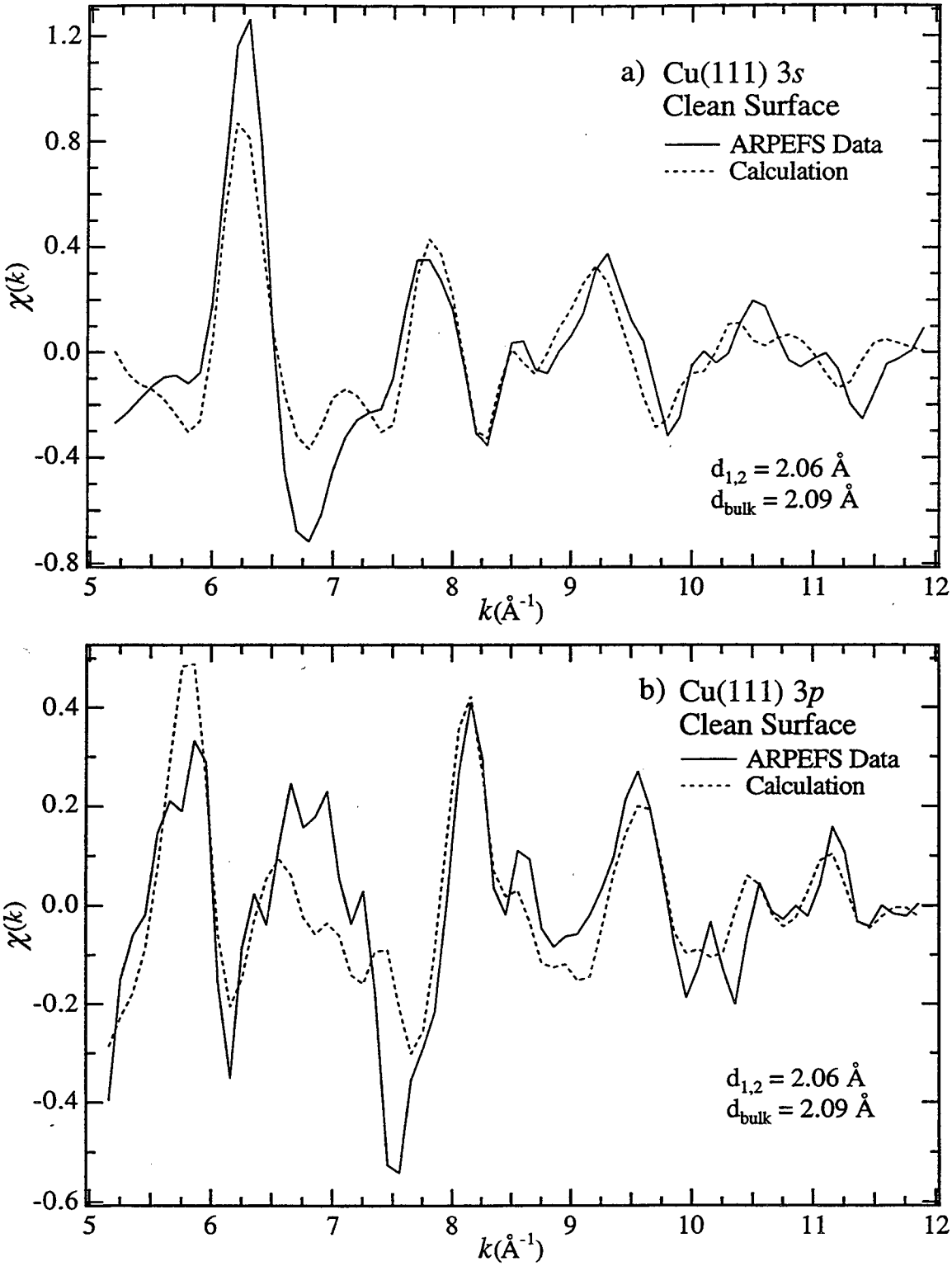

Figures 5a and 5b

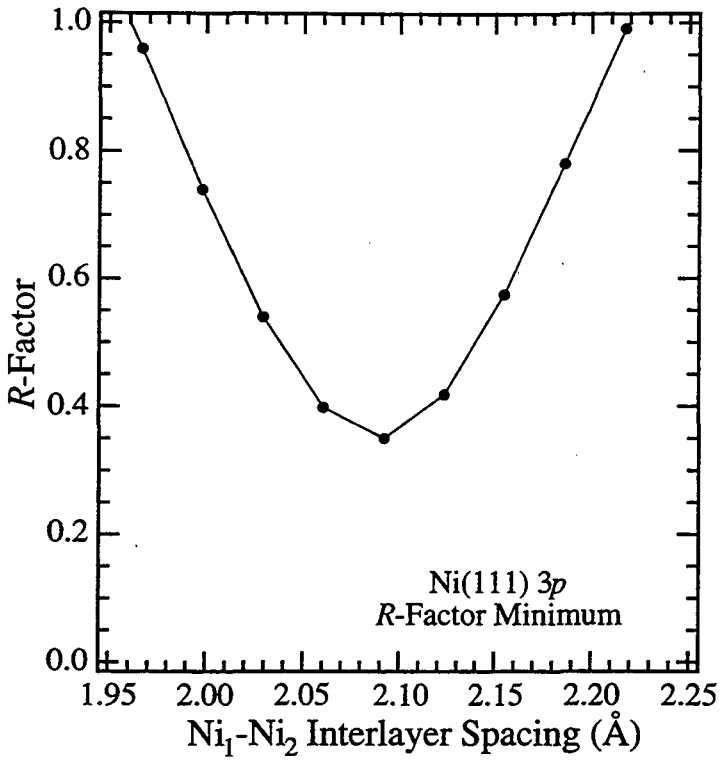
1.0
0.8
0.6
0.4
0.2
0.0
R-Factor
Ni(111) 3p
R-Factor Minimum
1.95
2.00
2.05
2.10
2.15
2.20
2.25
Ni1-Ni2 Interlayer Spacing (Å)

Figure 6

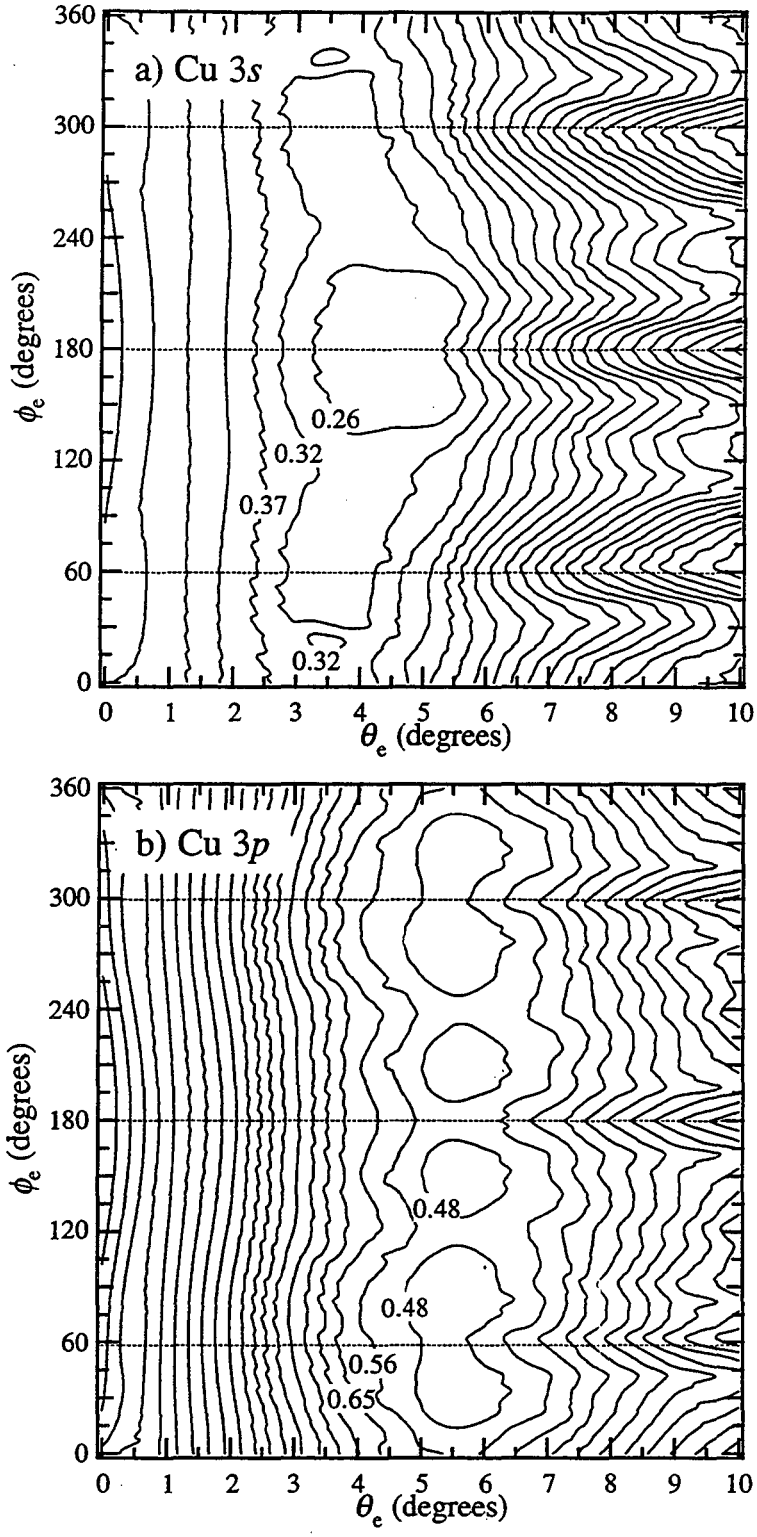

Figures 7a and 7b

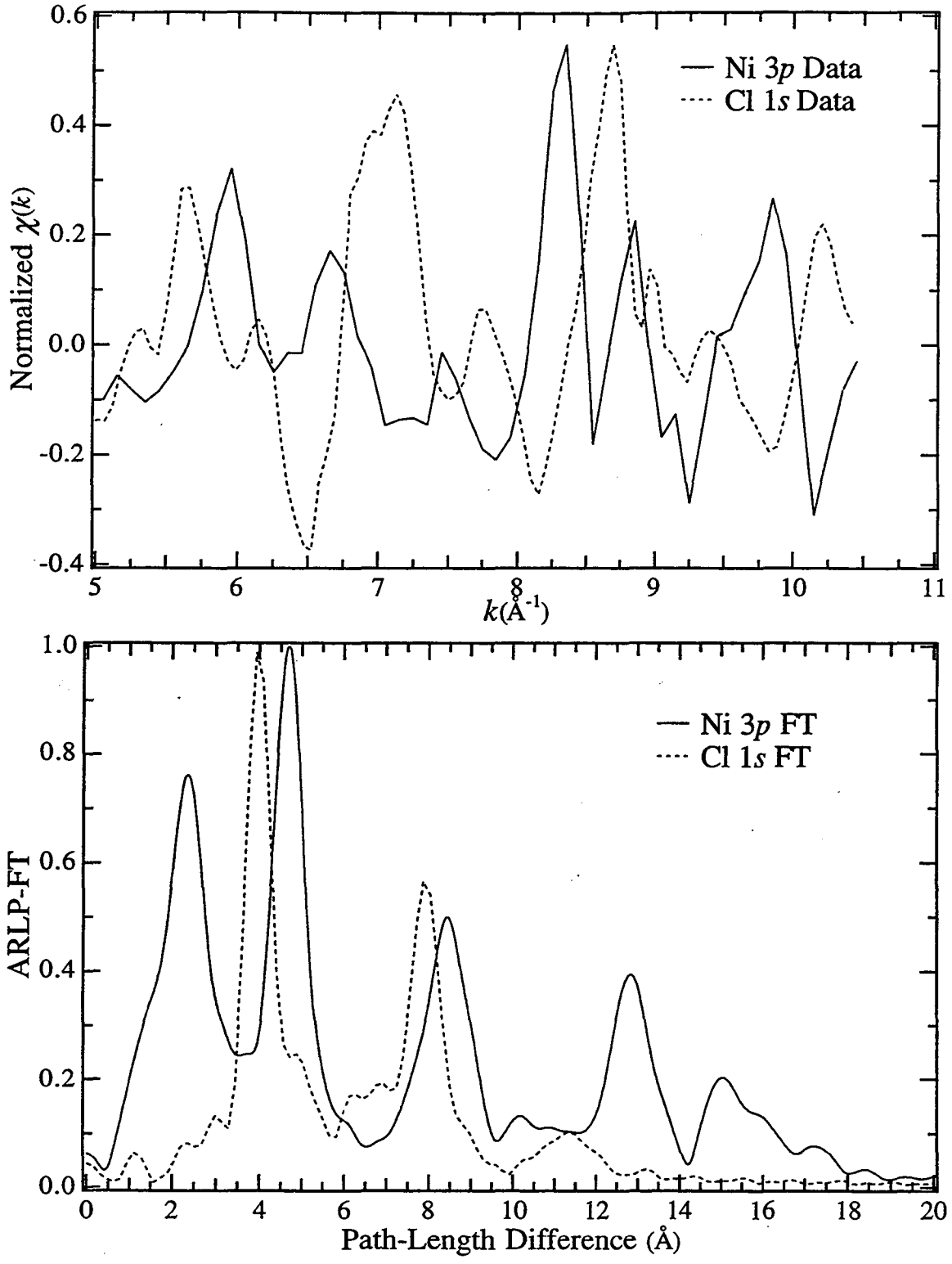
Ni 3p Data
Cl 1s Data
Normalized χ(k)
k(Å-1)
Ni 3p FT
Cl 1s FT
ARLP-FT
Path-Length Difference (Å)

Figure 8

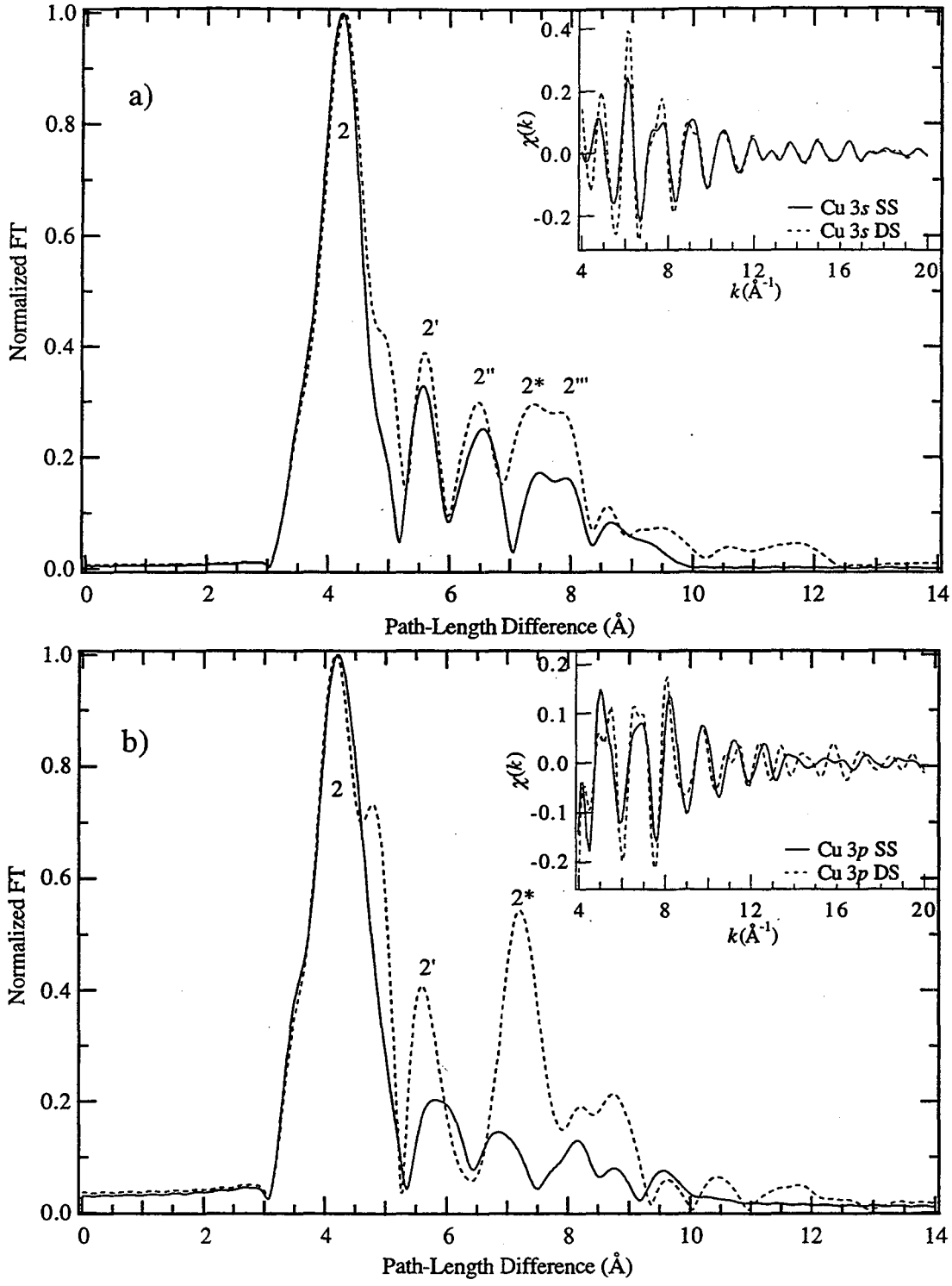

Figures 9a and 9b

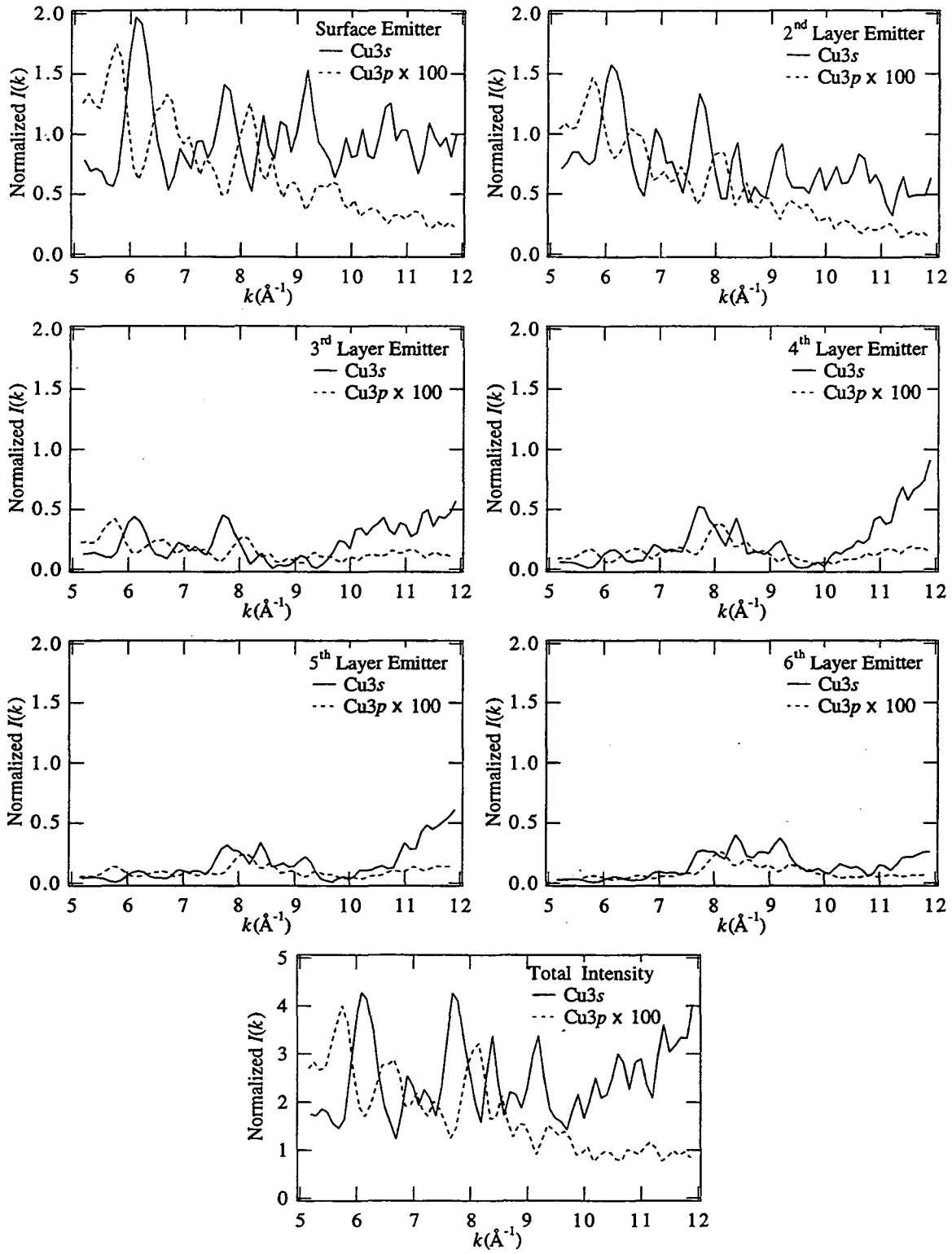
Surface Emitter
— Cu3s
--- Cu3p x 100
2nd Layer Emitter
— Cu3s
--- Cu3p x 100
3rd Layer Emitter
— Cu3s
--- Cu3p x 100
4th Layer Emitter
— Cu3s
--- Cu3p x 100
5th Layer Emitter
— Cu3s
--- Cu3p x 100
6th Layer Emitter
— Cu3s
--- Cu3p x 100
Total Intensity
— Cu3s
--- Cu3p x 100
Normalized I(k)
k(Å-1)

Figure 10

REFERENCES

1 S. D. Kevan, D. H. Rosenblatt, D. Denley, B. C. Lu, and D. A. Shirley, Phys. Rev. Lett. **41**, 1565 (1978).

2 J. J. Barton, C. C. Bahr, Z. Hussain, S. W. Robey, J. G. Tobin, L. E. Klebanoff, and D. A. Shirley, Phys. Rev. Lett. **51**, 272 (1983).

3 D. P. Woodruff, D. Norman, B. W. Holland, N. V. Smith, H. H. Farrell, and M. M. Traum, Phys. Rev. Lett. **41**, 1130 (1978).

4 M. Sagurton, E. L. Bullock, and C. S. Fadley, Surf. Sci. **182**, 287 (1987).

5 Y. Zheng and D. A. Shirley, Chem. Phys. Lett. **203**, 114 (1993).

6 J. J. Barton, C. C. Bahr, S. W. Robey, Z. Hussain, E. Umbach, and D. A. Shirley, Phys. Rev. B **34**, 3807 (1986).

7 S. W. Robey, C. C. Bahr, Z. Hussain, J. J. Barton, K. T. Leung, J. R. Lou, A. E. S. v. Wittenau, and D. A. Shirley, Phys. Rev. B **35**, 5657 (1987).

8 L. Q. Wang, A. E. S. v. Wittenau, Z. G. Ji, L. S. Wang, Z. Q. Huang, and D. A. Shirley, Phys. Rev. B **44**, 1292 (1991).

9 Z. Q. Huang, L. Q. Wang, A. E. S. v. Wittenau, Z. Hussain, and D. A. Shirley, Phys. Rev. B **47**, 13626 (1993).

10 Z. Q. Huang, Z. Hussain, W. T. Huff, E. J. Moler, and D. A. Shirley, Phys. Rev. B **48**, 1696 (1993).

11 Y. Zheng, E. Moler, E. Hudson, Z. Hussain, and D. A. Shirley, Phys. Rev. B **48**, 4960 (1993).

12 W. R. A. Huff, Y. Chen, X. S. Zhang, L. J. Terminello, F. M. Tao, Y. K. Pan, S. A. Kellar, E. J. Moler, Z. Hussain, H. Wu, Y. Zheng, X. Zhou, A. E. S. v. Wittenau, S. Kim, Z. Q. Huang, Z. Z. Yang, and D. A. Shirley, (to be published).

13 W. R. A. Huff, Y. Zheng, Z. Hussain, and D. A. Shirley, J. Phys. Chem. **98**, 9182 (1994).

14 J. C. Tang, Chin. Phys. Lett. **4**, 321 (1987).

15 S. Y. Tong and J. C. Tang, Phys. Rev. B **25**, 6526 (1982).

16 M. Biagini, Phys. Rev. B **48**, 2974 (1993).

17 S. D. Kevan, Ph. D. Thesis, Department of *Ph.D. Thesis*, The University of California, Berkeley at 1980.

18 Z. Hussain, W. R. A. Huff, S. A. Kellar, E. J. Moler, P. A. Heimann, W. McKinney, M. R. Howells, J. B. Kortright, M. A. Rice, C. Cummings, T. Lauritzen, J. P. McKean, S. C. Irick, F. J. Palomares, R. X. Ynzunza, Z. Wang, G. Andronaco, N. Hartman, E. D. Tober, H. Wu, Y. Zheng, A. Adamson, A. T. Young, H. Daimon, H. A. Padmore, C. S. Fadley, and D. A. Shirley, (Lawrence Berkeley National Laboratory, 1996).

19 J. J. Barton, S. W. Robey, and D. A. Shirley, Phys. Rev. B **34**, 778 (1986).

20 J. J. Barton, Ph. D. Thesis, Department of *Ph.D. Thesis*, The University of California, Berkeley at 1985.

21 J. J. Barton, Z. Hussain, and D. A. Shirley, Phys. Rev. B **35**, 933 (1987).

22 L. J. Terminello ,*Private Communication.*

23 J. J. Barton and D. A. Shirley, Phys. Rev. B **32**, 1892 (1985).

24 A. Kaduwela, Ph. D. Thesis, Department of *Ph.D. Thesis*, University of Hawaii at Manoa, Honolulu at 1991.

25 J. J. Rehr and R. C. Albers, Phys. Rev. B **41**, 8139 (1990).

26 D. J. Friedman and C. S. Fadley, J. Electron Spectrosc. Relat. Phenom. **51**, 689 (1990).

27 Y. Chen, H. Wu, and D. A. Shirley, , 1995).

28 S. M. Goldberg, C. S. Fadley, and S. Kono, J. Electron Spectrosc. Relat. Phenom. **21**, 285 (1981).

29 S. T. Manson and J. W. Cooper, Phys. Rev. **165**, 126 (1968).

30 V. L. Moruzzi, J. F. Janak, and A. R. Williams, *Calculated Electronic Properties of Metals* (Pergamon Press, Inc., New York, 1978).

31 R. E. Allen, G. P. Alldredge, and F. W. d. Wette, J. Chem. Phys. **54**, 2605 (1971).

32 S. Tanuma, C. J. Powell, and D. R. Penn, Surf. Interface Anal. **20**, 77 (1993).

33 S. P. Tear, K. Roll, and M. Prutton, J. Phys. C **14**, 3297 (1981).

34 S. A. Lindgren, L. Wallden, J. Rundgren, and P. Westrin, Phys. Rev. B **29**, 576 (1984).

35 W. H. Press, S. A. Teukolsky, W. T. Vetterling, and B. P. Flannery, *Numerical Recipes in Fortran: The Art of Scientific Computing* (University Press, Cambridge, 1992).

36 L.-Q. Wang, Z. Hussain, Z. Q. Huang, A. E. S. v. Wittenau, D. W. Lindle, and D. A. Shirley, Phys. Rev. B **44**, 13711 (1991).

37 B. L. Petersen, L. J. Terminello, J. J. Barton, and D. A. Shirley, Chem. Phys. Lett. **213**, 412 (1993).

Ernest Orlando Lawrence Berkeley National Laboratory
One Cyclotron Road | Berkeley, California 94720

Prepared for the U.S. Department of Energy under Contract No. DE-AC03-76SF00098